Uncovering Ocean Mixed Layer Dynamics from the Sea Surface State

Yidongfang Si[1], Leah Johnson[2], and Abigail Bodner[1,3]

[1]Department of Earth, Atmospheric and Planetary Sciences, Massachusetts Institute of Technology, Cambridge, MA
[2]Applied Physics Laboratory, University of Washington, Seattle, WA
[3]Department of Electrical Engineering and Computer Science, Massachusetts Institute of Technology, Cambridge, MA

Key Points:

- Buoyancy anomalies generated by ocean mixed layer eddies can be diagnosed through spatial filtering of sea surface height.
- Sea surface height gradient can be used to parameterize the vertical eddy buoyancy flux in the mixed layer.
- Mixed layer depth and vertical heat flux can be estimated from surface-observable quantities.

Corresponding author: Abigail Bodner, `abodner@mit.edu`

Abstract

Submesoscale dynamics strongly influence the upper ocean, regulating mixing, air–sea exchange, and vertical heat transport. The recent SWOT mission provides unprecedented high-resolution observations of sea surface height (SSH), yet linking these surface measurements to subsurface ocean dynamics remains challenging. We develop a theoretical framework for diagnosing key mixed layer properties from surface-observable states. We show that horizontal density anomalies induced by mixed-layer eddies produce surface imprints that can be effectively captured by spatially filtered SSH. The filtered SSH is integrated into the Mixed Layer Eddy parameterization to infer the effects of submesoscale restratification. A potential energy budget accounting for the mixing-restratification competition in the mixed layer is diagnosed from surface buoyancy flux, wind stress, and the SSH gradient, enabling reconstruction of the mixed-layer depth. Vertical eddy heat flux can be further reconstructed from the SSH gradient. This framework offers a promising approach for diagnosing interior submesoscale processes using surface observations.

Plain Language Summary

Ocean submesoscale flows, occurring at scales of roughly 1–30 km, are crucial for moving heat, carbon, and other materials vertically in the upper ocean. These flows affect how the ocean mixes and how it exchanges heat and gases with the atmosphere. Because direct observations are difficult and expensive, much of the subsurface ocean remains largely unexplored. The recently launched Surface Water and Ocean Topography (SWOT) satellite provides exceptionally detailed measurements of sea surface height. However, it is still challenging to use these observations to understand what is happening beneath the ocean's surface. This study reduced the gap by developing a theoretical framework that uses surface information to reveal important details about the subsurface, such as how deep the mixed layer is and how heat moves up and down. Submesoscale mixed-layer eddies—swirling motions in the well-mixed surface layer—are known to generate signals that can be detected from variations in sea surface height. By applying a spatial filter to remove large-scale signals, the surface signals created by these eddies can be used to reconstruct mixed layer depth and vertical heat flux. This method provides a practical way to estimate subsurface changes from surface states and can be applied to future observations.

1 Introduction

Submesoscale dynamics in the ocean mixed layer (ML) play a crucial role in regulating global heat and carbon uptake (Su et al., 2018; Guo et al., 2024), primary productivity (Mahadevan, 2016), and energy transfer (Taylor & Thompson, 2023; Srinivasan et al., 2023; Buckingham et al., 2019). Submesoscale fronts, characterized by strong horizontal density gradients, are typically driven by large-scale convergent flow (McWilliams, 2019; Yu et al., 2024). These fronts are often susceptible to baroclinic instability (Boccaletti et al., 2007), which gives rise to submesoscale eddies in the ML. Through slumping denser water beneath lighter water, the submesoscale eddies tilt isopycnals and act to restratify the ML (Fox-Kemper et al., 2008; Fox-Kemper & Ferrari, 2008). In addition, observations indicate that submesoscale eddies contribute substantially to upward vertical heat transport (Torres et al., 2025; Siegelman et al., 2020).

However, the dynamics and impacts of ML eddies are not fully understood. Despite the importance of submesoscale processes in the ML, fully resolving them requires a very high model resolution (Taylor & Thompson, 2023), resulting in substantial computational cost that limits both the duration and horizontal extent of numerical simulations. Moreover, although satellite observations (*e.g.*, sea surface temperature and salinity) and *in situ* measurements (*e.g.*, regional field campaigns and autonomous underwater vehicles) provide valuable insights into upper-ocean variability, their limited spatial

and temporal coverage hinders a comprehensive dynamical understanding of ML processes. The recent launch of the Surface Water and Ocean Topography (SWOT) satellite now enables global observations of high-resolution sea surface height (SSH), revealing ubiquitous submesoscale variability (Archer et al., 2025; X. Zhang & Callies, 2025; Z. Zhang et al., 2024). However, a critical gap remains in linking satellite observations to subsurface dynamics, in spite of recent efforts based on idealized theoretical models such as the surface quasi-geostrophic theory (Carli et al., 2024; Dù et al., 2025; Y. Zhang et al., 2025). Closing this gap would enable global diagnosis of ML processes from surface observations, which would be extremely valuable.

In this study, we develop a physically grounded framework to infer mixed layer depth (MLD) and vertical heat flux from surface-observable variables.

2 Key characteristics of submesoscale eddies in the Icelandic Basin

To demonstrate the applicability of the developed method, we select the Icelandic Basin as the test region, where previous observations indicate pronounced submesoscale activity, particularly during the spring restratification period (Johnson et al., 2016; Mahadevan et al., 2012). We use output from LLC4320, a 1/48° global ocean-sea ice simulation based on the MIT General Circulation Model (Marshall, Adcroft, et al., 1997; Marshall, Hill, et al., 1997), which has been widely used to investigate submesoscale dynamics (Su et al., 2018; Siegelman, 2020; Khatri et al., 2021). The model has vertical resolution ranging from 1.0 m to 41.5 m in the upper 800 m, and mean horizontal spacing of 1.13 km in the selected region. For details of the model configuration, we refer the reader to Gallmeier et al. (2023).

Fig. 1(a) shows the location of the domain. From late November to early March, a strong net surface buoyancy flux, dominated by surface cooling, drives deepening of the ML base (Fig. 1b). During spring (March to May), the ML re-stratifies, as indicated by shoaling of the ML and increased ML stratification. In summer, surface heating maintains a shallow ML throughout the season. Fig. 1(c)–(h) show the surface vorticity ζ, strain rate σ, and horizontal divergence Δ, which are commonly used to quantify the intensity of submesoscale motions (Balwada et al., 2021), where

$$\zeta = v^s_x - u^s_y, \quad \sigma = \sqrt{(u^s_x - v^s_y)^2 + (v^s_x + u^s_y)^2}, \quad \Delta = u^s_x + v^s_y, \tag{1}$$

the superscripts $\cdot^s$ denote surface fields, and the subscripts represent partial derivatives. Each field is normalized by the domain-averaged Coriolis parameter $f_0 = 1.27\times10^{-4}\,\mathrm{s}^{-1}$. Surface eddy activity exhibits strong seasonality in this region, with pronounced submesoscale activity in winter and spring, and weaker mesoscale eddies during summer and autumn.

Baroclinic instability of submesoscale fronts in the ML generates submesoscale eddies (Boccaletti et al., 2007), which induce overturning circulations that adiabatically slump the fronts (Fox-Kemper et al., 2008), converting horizontal density gradients into vertical stratification. Therefore, the agreement between horizontal and vertical Turner angles can be used to identify periods when frontal slumping by these eddies dominates the ML restratification, as the Turner angles quantify the relative contributions of temperature and salinity to density (Johnson et al., 2016). Assuming a linear equation of state, the potential density can be approximated as

$$\rho = \rho_0\Big[1 - \alpha(\theta - \theta_0) + \beta(S - S_0)\Big], \tag{2}$$

where α is the thermal expansion coefficient, β is the haline contraction coefficient, θ_0 is the reference temperature, and S_0 is the reference salinity. Following Johnson et al.

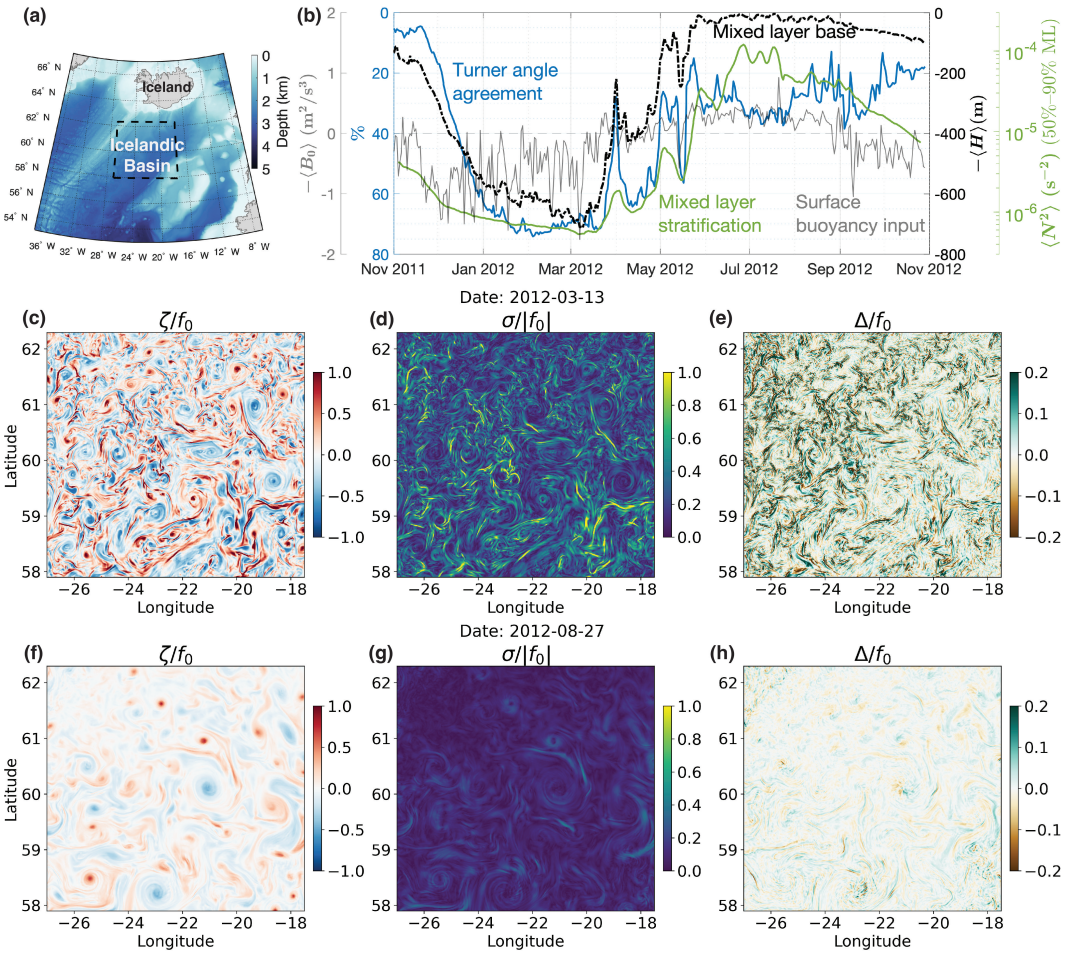

Figure 1. (a) Seafloor bathymetry with the Icelandic Basin highlighted by a black dashed box (27°W–17.5°W, 57.9°N–62.3°N). (b) Timeseries of the domain-averaged net surface buoyancy input (gray), vertical position of the ML base (equal to $-\langle H \rangle$) (black), mean stratification averaged over 50%–90% of the MLD (green), and percentage of Turner angle differences less than 10° (blue). (c-h) Daily-averaged surface vorticity, strain rate, and horizontal divergence normalized by the Coriolis parameter, for early spring (c-e; Mar 13th, 2012) and late summer (f-h; Aug 27th, 2012).

(2016), we define the horizontal and vertical Turner angles as

$$\mathrm{Tu}_h = \arctan\left[\frac{\alpha\partial_n\theta^s + \beta\partial_n S^s}{\alpha\partial_n\theta^s - \beta\partial_n S^s}\right], \quad \mathrm{Tu}_v = \arctan\left[\frac{\alpha\partial_z\theta + \beta\partial_z S}{\alpha\partial_z\theta - \beta\partial_z S}\right], \tag{3}$$

where

$$\partial_n = \frac{\nabla_h\rho}{|\nabla_h\rho|}\cdot\nabla_h \tag{4}$$

denotes the horizontal cross-isopycnal gradient, and $\nabla_h = (\partial_x, \partial_y)$ represents the horizontal gradient operator. We quantify the agreement between the horizontal and vertical Turner angles using the percentage of the absolute Turner angle difference less than 10°. As shown in Fig. 1(b), the two Turner angles agree relatively well during winter and early spring (January–April), indicating the prevalence of submesoscale fronts and suggesting that ML restratification in early spring largely results from frontal slumping, consistent with observations by Johnson et al. (2016).

3 Diagnosing mixed layer steric height from submesoscale SSH

We hypothesize that ML eddies imprint detectable signatures on SSH at submesoscale wavelengths. This hypothesis is motivated by previous findings that vertically integrating the global *in-situ* density anomaly over the upper 2,000 m of the ocean yields a steric height estimate that closely tracks variations in SSH (Delman, 2025). Such an approach primarily captures large-scale circulation and mesoscale eddies, which can extend into the deep ocean. In addition, Wang et al. (2025) show that in the California current region, the SSH anomaly captured by SWOT, which resolves submesoscale variability, closely matches the steric height anomaly derived from mooring measurements in the upper 500 m after removing barometric and barotropic effects (their Fig. 2). Below, we adopt a similar approach but consider only the density variations within the ML. We examine whether variations in ML steric height can be inferred from SSH anomalies, provided that the contributions from large-scale circulation and mesoscale eddies are filtered out.

We define the MLD as the depth at which the potential density exceeds the surface density by a criterion of $\Delta\rho = 0.03\,\mathrm{kg/m^3}$. By definition, destruction of stratification in the mixed layer (*e.g.*, by increased mixing) is inversely related to the deepening of the mixed layer, *i.e.*,

$$\overline{\partial_z b}^z = \frac{g\Delta\rho}{\rho_0}\frac{1}{H}, \tag{5}$$

where $b = -g(\rho-\rho_0)/\rho_0$ is buoyancy, ρ is potential density, $\rho_0 = 1027.5\,\mathrm{kg/m^3}$ is the reference density, $g = 9.81\,\mathrm{m/s^2}$ is the gravitational acceleration, H is the MLD, and the overline $\overline{\cdot}^z$ denotes ML averages

$$\overline{\cdot}^z = \frac{1}{H}\int_{-H}^{0}\cdot\, dz. \tag{6}$$

This definition of MLD differs slightly from the canonical one (de Boyer Montégut et al., 2004; Treguier et al., 2023), which uses 10 m depth as a reference level to reduce the influence of diurnal warming/cooling on MLD estimates. After removing the diurnal cycle by taking daily averages, we find that the two definitions produce nearly identical domain-averaged MLD (Fig. S1). When computing ML averages, we additionally exclude regions where the MLD is shallower than 10 m in all analysis. Note that, after taking domain averages, the results are not sensitive to either the definition of the MLD, or the exclusion of regions with $H < 10\,\mathrm{m}$.

3.1 Mixed layer steric height

We define the ML steric height as the vertical integral of the *in-situ* density anomaly over the ML following Eq. 1 of Wang et al. (2025).

$$\eta_{\text{steric}} = -\frac{1}{\rho_0}\int_{-\langle H\rangle}^{0} \rho'_{\text{in situ}}\, dz, \tag{7}$$

where the angle brackets $\langle\cdot\rangle$ denote horizontal average over the domain of interest, the *in-situ* density anomaly is defined as the departure from the domain-averaged value

$$\rho'_{\text{in situ}} = \rho_{\text{in situ}} - \langle\rho_{\text{in situ}}\rangle, \quad \langle\cdot\rangle = \frac{1}{L_x L_y}\int_0^{L_x}\int_0^{L_y} \cdot\, dx\, dy, \tag{8}$$

and L_x and L_y denote the horizontal domain sizes.

Fig. 2 shows the SSH anomaly (a) and η_{steric} (b). Because the ML is deeper in the northwest of the domain and shallower in the southeast, integrating density anomalies from the domain-averaged ML base produces higher η_{steric} in the southeast. This, however, does not affect our results, as our analysis focuses on the gradient of η_{steric}, which is dominated by small-scale local density variations. We retain the definition of η_{steric} using the domain-averaged MLD for three reasons: (i) it has negligible impact on the gradient magnitudes, (ii) it yields a simpler form for the ML eddy parameterization using steric height; and (iii) it aligns better with the eddy parameterizations employed in coarse-resolution climate models, where small-scale variations in the MLD are not resolved.

We assume that, once internal waves are temporally filtered out in the daily averages, the horizontal gradient of ML steric height is dominated by the variations in temperature and salinity, rather than pressure. Under this assumption, the effects of horizontal pressure gradients in the ML are small, such that the horizontal gradient of the *in-situ* density $\rho_{\text{in situ}}$ can be approximated by that of the potential density ρ. Therefore, the horizontal gradient of the ML steric height can be approximated as

$$\nabla_h\eta_{\text{steric}} \equiv -\frac{1}{\rho_0}\int_{-\langle H\rangle}^{0} \nabla_h\rho'_{\text{in situ}}\, dz \approx -\frac{1}{\rho_0}\int_{-\langle H\rangle}^{0} \nabla_h\rho\, dz \approx -\frac{1}{\rho_0}\overline{\nabla_h\rho}^{z}\langle H\rangle = \frac{1}{g}\overline{\nabla_h b}^{z}\langle H\rangle, \tag{9}$$

which shows that $\nabla_h\eta_{\text{steric}}$ scales with the ML-averaged horizontal buoyancy gradient multiplied by the domain-averaged MLD.

In the following analysis, we apply a mesoscale filter that effectively removes large-scale pressure anomalies. As a result, our method is likely insensitive to large-scale pressure anomalies at depth, even when internal waves cannot be removed through daily averaging (*e.g.*, when applied to the SWOT data).

3.2 Submesoscale sea surface height anomaly

In order to isolate the signal associated with submesoscale eddies, we apply a Gaussian filter to SSH to remove the large-scale flow, including mesoscale eddies, following Uchida et al. (2022). To account for the seasonal variability of ML eddy scales, this Gaussian filter scale is determined by the time-varying wavelength of the most unstable ML-instability mode (Stone, 1970):

$$\lambda_{\text{MLI}} = \frac{2\pi}{\sqrt{5/2}} L_d\sqrt{1 + Ri_b^{-1}}, \tag{10}$$

where $L_d = \overline{N}^{z} H/f$ is the ML radius of deformation, $N = \sqrt{\partial_z b}$ is the buoyancy frequency, f is the Coriolis parameter, $Ri_b = \overline{N^2 f^2/|\nabla_h b|^2}^{\text{hm},\,z}$ is the balanced Richardson number, with $\overline{\cdot}^{\text{hm},\,z}$ denoting the harmonic mean in the vertical direction to emphasize the influence of small local Richardson numbers. In this region, λ_{MLI} peaks in

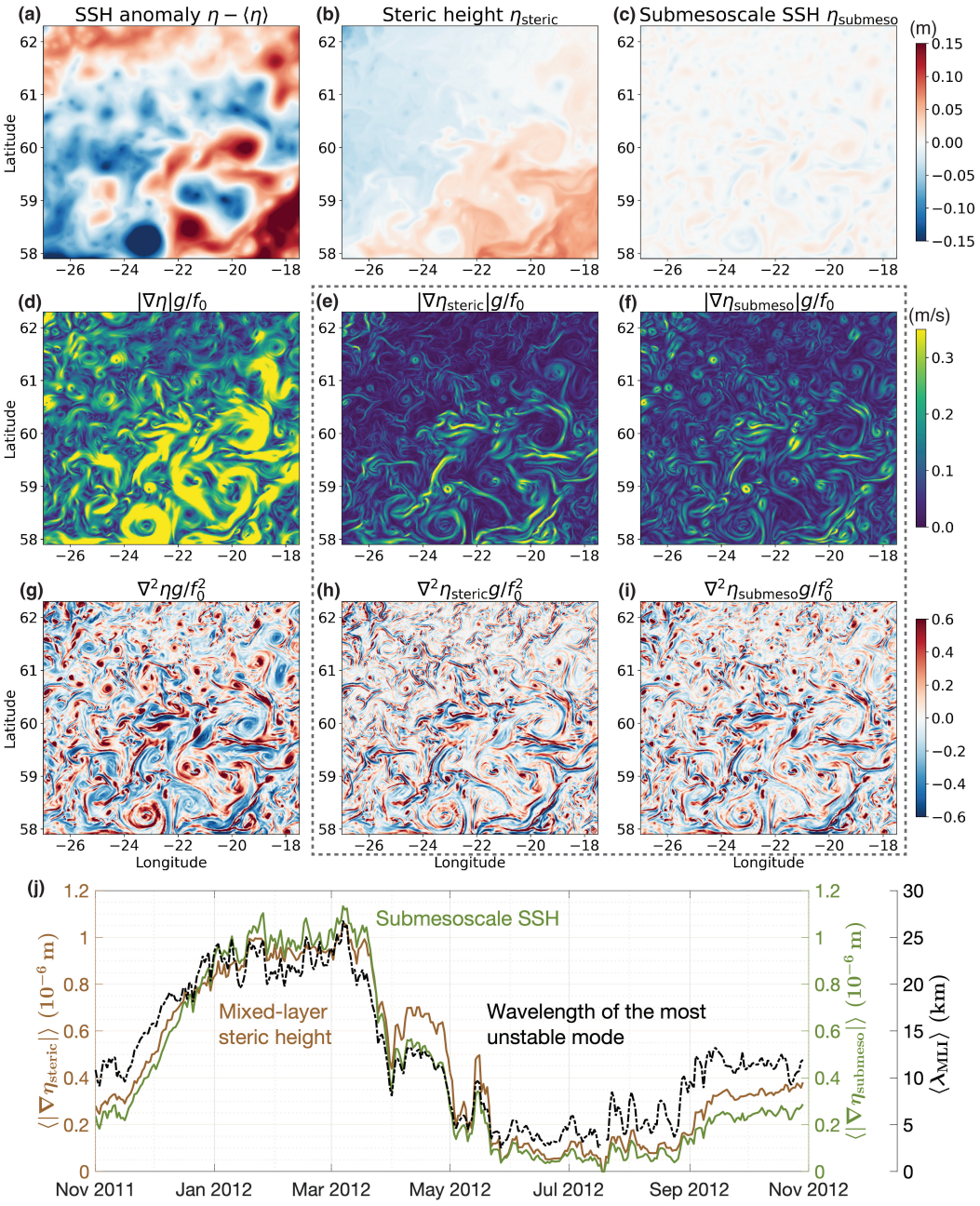

Figure 2. Daily-averaged (a) SSH anomaly, (b) ML steric height, and (c) submesoscale SSH anomaly on Feb 15th, 2012. (d-f): Gradient magnitude of the first row, normalized by f_0/g to obtain the unit of velocity (m/s). (g-i): Laplacian of the first row, normalized by f_0^2/g to obtain the Rossby number (dimensionless). (j) Timeseries of daily- and domain-averaged gradient magnitude of ML steric height (brown) and submesoscale SSH (green), along with the wavelength of the most unstable ML instability mode λ_{MLI} (black).

winter and early spring, and reaches its seasonal minimum during summer (Figs. 2j and S2, Text S2), consistent with Dong et al. (2020).

We filter the SSH field at the scale $L_{\mathrm{MLI}} = 0.8\langle\lambda_{\mathrm{MLI}}\rangle$ (hereafter referred to as the submesoscale SSH). The factor 0.8 is chosen so that the resulting submesoscale SSH is better aligned with the steric height.

$$\eta_{\mathrm{submeso}}(x,y,t) = \eta'(x,y,t) - \int_0^{L_x}\int_0^{L_y} \eta'(x',y',t)\frac{1}{2\pi\sigma^2}e^{-\frac{(x-x')^2+(y-y')^2}{2\sigma^2}}dx'dy', \tag{11}$$

where $\eta' = \eta - \langle\eta\rangle$ is the SSH anomaly, L_{MLI} is prescribed as the Gaussian full width at half maximum, and $\sigma = L_{\mathrm{MLI}}/(2\sqrt{2\ln 2})$ is the corresponding standard deviation. Fig. 2(b–c) shows some mismatch between submesoscale SSH and ML steric height, arising because the definition of η_{steric} neglects horizontal variations in MLD (Text S1). However, this has negligible impact on the gradients.

Fig. 2(c–d) shows that the horizontal gradient of submesoscale SSH closely matches that of the ML steric height:

$$\nabla_h\eta_{\mathrm{submeso}} \approx \nabla_h\eta_{\mathrm{steric}}. \tag{12}$$

The results remain robust when a constant filter scale is used for σ in place of the time-varying scale L_{MLI}, particularly during seasons of pronounced submesoscale activity (Fig. S3, Text S3). The Rossby number estimated from submesoscale SSH is also in close agreement with that derived from steric height (Fig. 2h–i). Combining Eq. 12 with Eq. 9, we obtain that

$$g\nabla_h\eta_{\mathrm{submeso}} \approx \overline{\nabla_h b}^{z}\langle H\rangle. \tag{13}$$

This relation will be used later to reconstruct the evolution of MLD and estimate ML-averaged vertical heat flux from ocean surface states.

4 Estimating mixed layer depth from submesoscale SSH

Building on the results of the previous section, we derive a theoretical framework for reconstructing MLD using surface variables.

4.1 Volume-averaged potential energy budget

Inspired by previous studies (Eq. 14 of Thompson et al. (2016); Eq. 3 of Johnson et al. (2020); Eq. 5 of Fox-Kemper et al. (2008)), we consider a volume-averaged potential energy (PE) budget for the surface ML. We decompose the change of ML potential energy into four contributions: (i) net surface buoyancy flux B_0, (ii) Ekman buoyancy flux B_{Ek}, (iii) frontal slumping by eddy buoyancy flux B_{eddy}, and (iv) a residual term, including the effects of horizontal advection through the lateral boundaries, turbulent mixing at the ML base, vertical advection by internal gravity waves, frontogenesis and frontolysis, *etc.*

$$\frac{\partial}{\partial t}\mathrm{PE} = \left\langle B_0 + B_{\mathrm{Ek}} + B_{\mathrm{eddy}}\right\rangle + \mathrm{Residual}^{\mathrm{PE}}. \tag{14}$$

Following Sec. 3 of Fox-Kemper et al. (2008) and applying Eq. 5,

$$\mathrm{PE} \equiv \left\langle \overline{-zb}^{z}\right\rangle \propto \langle H\rangle^2\left\langle\overline{\partial_z b}^{z}\right\rangle \approx \frac{g\Delta\rho}{\rho_0}\langle H\rangle, \tag{15}$$

Therefore, the volume-averaged PE budget in Eq. 14 can be expressed as a budget for the MLD:

$$\frac{\partial\langle H\rangle}{\partial t} = \frac{\rho_0}{g\Delta\rho}\left\langle B_0 + B_{\mathrm{Ek}} + B_{\mathrm{eddy}}\right\rangle + \mathrm{Residual}, \tag{16}$$

which resembles the ML model presented in Johnson et al. (2023) (their Eqs. A1–A2) and Kraus and Turner (1967), but includes an additional term representing the effects of ML eddies.

4.2 Net surface buoyancy flux

Following Marshall and Schott (1999), the net surface buoyancy flux can be written in terms of the net heat and freshwater fluxes:

$$B_0 = -\frac{g\alpha}{\rho_0 C_p} Q_{\text{heat}} - \frac{g\beta S_0}{\rho_0} Q_{\text{fresh}}, \tag{17}$$

where $C_p = 3995\,\text{J/kg/K}$ is the specific heat capacity, $S_0 = 35.2\,\text{psu}$ is the reference surface salinity, Q_{heat} is the net surface heat flux (Fig. S4b), and Q_{fresh} is the net surface freshwater flux (Fig. S4c). Here, positive B_0 (surface buoyancy loss) corresponds to an increase in the volume-averaged PE or a deepening of the MLD, typically associated with surface cooling ($Q_{\text{heat}} < 0$). Consistent with observations in the Icelandic Basin (Johnson et al., 2020), the surface buoyancy flux in the LLC4320 in this region is primarily controlled by the surface heat flux, while the effect of the surface freshwater flux is negligible (Fig. S4).

4.3 Ekman buoyancy flux

Wind stress can generate or destruct ML stratification (Fig. 1 of Thomas and Ferrari (2008)) by the Ekman buoyancy flux, which can be estimated as the product of the Ekman transport and the surface horizontal buoyancy gradient ($\nabla_h b^s$) (*e.g.*, Thomas et al. (2013); Thompson et al. (2016))

$$B_{\text{Ek}} \approx \frac{\vec{\tau} \times \hat{\mathbf{z}}}{\rho_0 f} \cdot \nabla_h b^s \tag{18}$$

where $\hat{\mathbf{z}}$ is the upward unit vector, $\vec{\tau} = (\tau^x, \tau^y)$ is the wind stress, and b^s denotes surface buoyancy. In Eq. 18, using the depth-averaged horizontal buoyancy gradient over the ML, rather than the surface buoyancy gradient, yields qualitatively similar results (Text S4).

The contribution of the wind to the changes in the ML stratification can be either positive or negative, depending on the relative orientation of the surface winds and submesoscale fronts in the ocean (Thomas & Lee, 2005; Thomas & Ferrari, 2008). Glider observations suggest that the magnitude of the Ekman buoyancy flux is generally smaller than, but still comparable to, the eddy-induced buoyancy flux (*e.g.*, Fig. 11b of Thompson et al. (2016)). We will show later that when averaged over a broad region containing many fronts with varying orientation relative to the winds, the mean Ekman buoyancy flux largely cancels out and becomes much weaker than the net surface buoyancy flux and the eddy buoyancy flux. The resulting domain-mean contribution by Ekman buoyancy flux is positive, indicating that on overage, wind stress tends to deepen the ML. Note that, because the model cannot represent coupled air–sea dynamics, the Ekman buoyancy flux might be underestimated owing to the lack of nonlinear air–sea interactions, although current feedback may act to reduce the magnitude of Ekman buoyancy flux (Wenegrat, 2023).

4.4 Eddy vertical buoyancy flux

On average, submesoscale eddies act to re-stratify the ML. This effect is represented by a depth-averaged ML eddy vertical buoyancy flux. Following Uchida et al. (2022), we diagnose the eddy-induced vertical buoyancy flux as

$$B_{\text{eddy}} = -\overline{w'b'}^{z} \equiv -\overline{(w-\tilde{w})(b-\tilde{b})}^{z}, \tag{19}$$

where $\tilde{\cdot}$ denotes a 30-km lateral Gaussian filter. This filter scale needs to be larger than the most unstable wavelength of ML instability, as energy injection in the mixed layer occurs at larger scales (Z. Zhang et al., 2025), resulting from ML instability, transitional-layer instability, or mesoscale eddies (Text S5).

The change in ML potential energy due to submesoscale eddies can be parameterized as (Eq. 5 of Fox-Kemper et al. (2008); Eqs. 2–4 of Fox-Kemper and Ferrari (2008))

$$\langle -w'b' \rangle \approx -\frac{C_e \mu(z)}{|f|} \langle H \rangle^2 \langle \overline{\nabla_h b}^z \rangle^2 \tag{20}$$

where $C_e = 0.06$ is the recommended coefficient value, and $\mu(z)$ is a vertical structure function that peaks in the interior of the ML and decreases to zero at both the ocean surface and the base of the ML (Eq. 21 of Fox-Kemper et al. (2008)). To represent the eddy buoyancy flux averaged over the ML, we compute the ML average of the vertical structure function,

$$\mu_0 = \overline{\mu(z)}^z = \frac{1}{H} \int_{z=-H}^{z=0} \left[1 - \left(\frac{2z}{H} + 1\right)^2\right] \left[1 + \frac{5}{21}\left(\frac{2z}{H} + 1\right)^2\right] dz = \frac{44}{63}. \tag{21}$$

Taking the ML vertical average of Eq. 20 and Substituting Eq. 9 ($\langle H \rangle \overline{\nabla_h b}^z \approx g \nabla_h \eta_{\text{steric}}$) into the resulting expression gives

$$\left\langle B_{\text{eddy}} \right\rangle \approx \left\langle -\frac{C_e \mu_0 g^2}{|f|} \left|\nabla_h \eta_{\text{steric}}\right|^2 \right\rangle \approx \left\langle -\frac{C_e \mu_0 g^2}{|f|} \left|\nabla_h \eta_{\text{submeso}}\right|^2 \right\rangle. \tag{22}$$

Note that this term is always negative, indicating that eddies always act to decrease the volume-averaged ML potential energy, or equivalently, to shoal the ML.

4.5 Governing equation for mixed layer depth

By substituting Eqs. 17, 18, 22 into Eq. 16, we obtain an equation for the evolution of MLD:

$$\begin{aligned} \frac{\partial}{\partial t}\langle H \rangle &\approx \frac{\rho_0}{g \Delta \rho} \left\langle B_0 + B_{\text{Ek}} - \frac{C_e \mu_0 g^2}{|f|} |\nabla_h \eta_{\text{steric}}|^2 \right\rangle + \text{Residual} \\ &\approx \frac{\rho_0}{g \Delta \rho} \left\langle B_0 + B_{\text{Ek}} - \frac{C_e \mu_0 g^2}{|f|} |\nabla_h \eta_{\text{submeso}}|^2 \right\rangle + \text{Residual} \end{aligned} \tag{23}$$

When the residual term is small, this equation allows us to infer the MLD given surface heat flux, wind stress, and SSH anomaly.

The contribution of each term to the change in the domain-averaged MLD is shown in Fig. 3 (a). A positive tendency (black, $\partial_t \langle H \rangle$) indicates ML deepening, whereas a negative tendency indicates ML shoaling. Strong surface cooling acts to deepen the ML from November to March. Surface wind forcing contributes to ML deepening throughout the year, but its effect is much weaker than that of surface cooling. The diagnosed eddy-induced vertical buoyancy flux (VBF) is shown in purple, and the parameterized eddy fluxes by submesoscale SSH and steric height are shown in green and brown, respectively. Consistent with Eq. 22, the eddy-related terms are always negative, indicating that the ML eddies always act to shoal the ML.

The light pink curve represents the difference between the total tendency and the terms associated with surface forcing (labeled as the "horizontal" term). It represents the effects of horizontal eddy restratification and other processes, such as lateral advection through the domain boundaries. When the eddy-related terms (purple, green, and brown) align with the pink curve, the residual term is small, indicating that the theoretical framework performs well. However, during summer, despite strong surface heating and very weak eddy restratification, the MLD remains shallow and nearly constant. This suggests that other processes, such as turbulent mixing and entrainment, may contribute to balance the surface heating. Because our theory is designed for periods when ML eddies are pronounced, we leave a detailed analysis of the summertime MLD budget to future work.

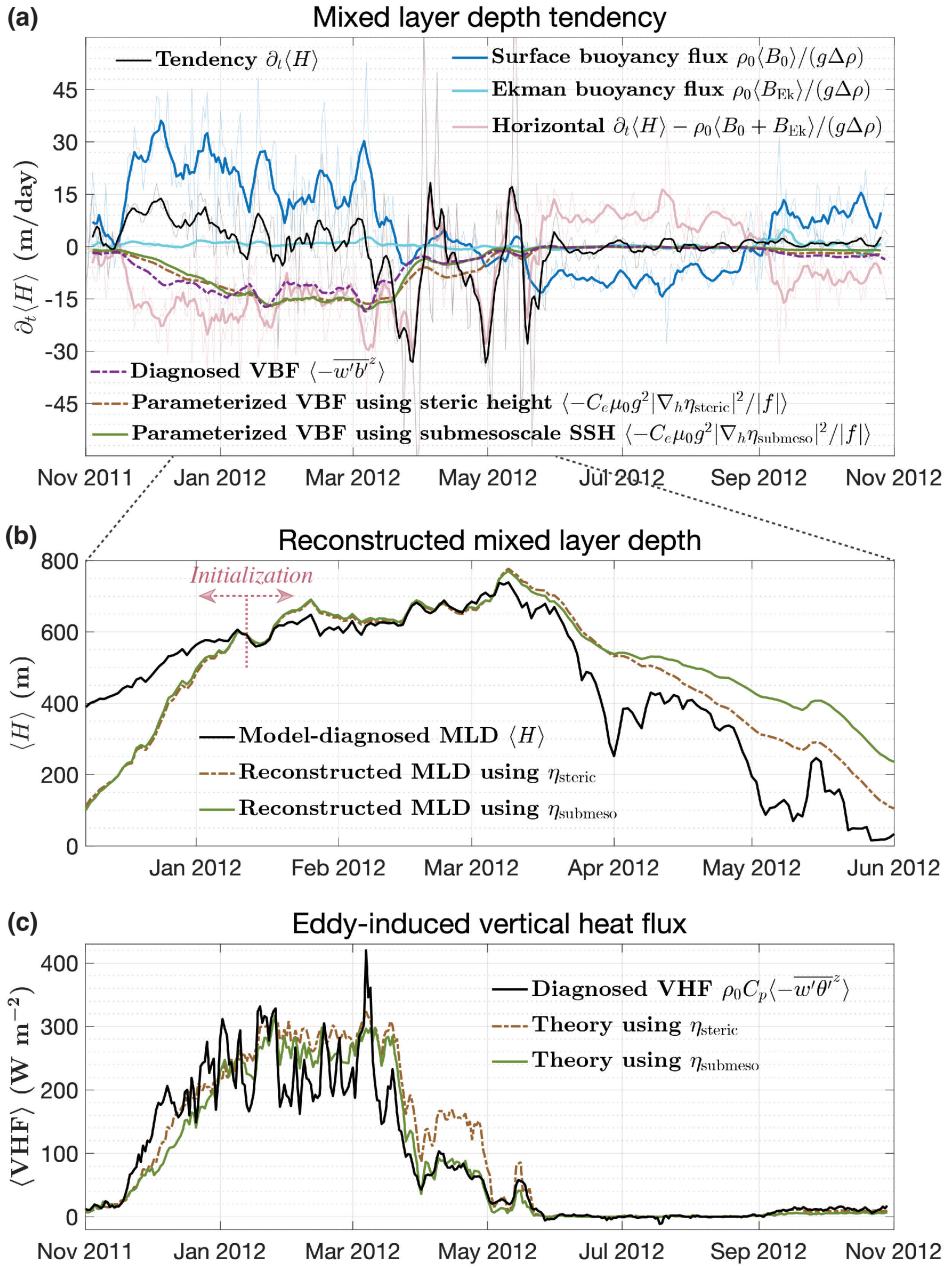

Figure 3. (a) MLD tendency, with thin semi-transparent lines representing daily values and thick lines showing weekly rolling means. (b) Domain-averaged MLD diagnosed from the model compared with the reconstructed MLD derived from ML steric height and submesoscale SSH. The pink dotted line indicates the initialization date (January 12th, 2012), at which the reconstructed MLD is matched to the diagnosed MLD. From this point, the theory-predicted MLD tendency is integrated both forward and backward in time. (c) Timeseries of daily-averaged model-diagnosed and theoretically reconstructed eddy-induced vertical heat flux.

Fig. 3 (a) shows that, from January to May, variations in the MLD are primarily controlled by the competition between surface forcing and ML eddy restratification. This balance allows us to reconstruct the MLD during this period by integrating Eq. 23 forward and backward in time, from a selected initialization date. Fig. 3 (b) shows the reconstructed MLD with an initialization date of Jan 12th, 2012. This initialization data is selected because the horizontal and vertical Turner angles begin to agree well (Fig. 1b), indicating that eddy activity becomes important in the MLD budget. Although errors accumulate with time, the difference between the reconstructed and diagnosed MLD remains within 8% (or $< 50\,\mathrm{m}$, relative to the MLD exceeding 600 m) for most of the period from January through the end of March.

Frontogenesis and frontolysis can also influence the MLD. Scaling analysis in Thomas and Ferrari (2008) (their Eq. 21) suggests that, typically, the influence of frontogenesis on the stratification of the surface ML can be on the same order of magnitude as wind forcing. However, we find that the Ekman buoyancy flux is much smaller than the surface heat flux and eddy buoyancy flux (Fig. 3a), and the contribution of frontogenesis or frontolysis in LLC4320 is also expected to be small due to insufficient resolution and the lack of coupled air–sea dynamics.

5 Estimating vertical heat flux from submesoscale SSH

The effects of ML eddies can be represented by an overturning circulation that acts to flatten sloping density surfaces, restratifying the ML (Fox-Kemper et al., 2008). This circulation transports warm water upward and cold water downward, producing an eddy-induced vertical heat flux (VHF).

In this section, we modify the submesoscale VHF parameterization using the surface density ratio and submesoscale SSH. This approach has potential observational applications: given satellite-observed surface temperature and salinity, together with submesoscale SSH from SWOT, the VHF could be estimated.

We diagnose the submesoscale eddy-induced VHF following the same approach as for the vertical buoyancy flux (Eq. 19),

$$\mathrm{VHF}_{\mathrm{diagnosed}} = \rho_0 C_p \overline{w'\theta'}^{z} = \rho_0 C_p \overline{(w-\tilde{w})(\theta-\tilde{\theta})}^{z} \tag{24}$$

To parameterize the VHF using only surface variables, we use a buoyancy ratio r to quantify the relative contributions of temperature and salinity to buoyancy, relating the magnitude of the cross-isopycnal temperature gradient to the buoyancy gradient as

$$\partial_n \theta = r \frac{\partial_n b}{\alpha g}. \tag{25}$$

Assuming a linear equation of state $\partial_n b = g(\alpha \partial_n \theta - \beta \partial_n S)$, the buoyancy ratio can be written as $r = R/(R-1)$, where $R = \alpha \partial_n \theta / \beta \partial_n S$ is the traditionally defined density ratio (Johnson et al., 2020). Both r and R are physically analogous to the horizontal Turner angle (Eq. 3). We use the buoyancy ratio here because it is easier to interpret physically.

Following Eqs. 2-3 of Fox-Kemper and Ferrari (2008), the overturning streamfunction induced by ML eddies is given by

$$\Psi = \frac{C_e \mu(z)}{|f|} H^2 \overline{\partial_n b}^{z}. \tag{26}$$

Below, we compute the submesoscale eddy-induced vertical heat flux using the similar framework as previous studies (*e.g.*, Eqs. 4-5 of Spungin et al. (2025); Eq. 5 of Biddle

and Swart (2020)), and set the vertical structure function $\mu(z) = \mu_0 = 44/63$ to represent its mean value throughout the ML (Eq. 21). We additionally substitute the horizontal temperature gradient with the expression given in Eq. 25. The vertical heat flux is

$$\begin{aligned} \mathrm{VHF_{MLE}} = \rho_0 C_p \Psi \overline{\partial_n \theta}^z &= \frac{\rho_0 C_p C_e \mu_0}{|f|} H^2 \overline{\partial_n b}^z \overline{\partial_n \theta}^z \\ &= \frac{\rho_0 C_p C_e \mu_0}{\alpha g |f|} H^2 \overline{\partial_n b}^z \, \overline{r \, \partial_n b}^z \\ &\approx \frac{\rho_0 C_p C_e \mu_0}{\alpha g |f|} H^2 \left| \overline{\nabla_h b}^z \right|^2 r^s \end{aligned} \tag{27}$$

Note that, in the equation above, we assume that the buoyancy ratio r remains approximately constant with depth throughout the ML and can therefore be represented by its surface value r^s. In addition, we have replaced the squared horizontal cross-isopycnal buoyancy gradient ($|\partial_n b|^2$) with the squared magnitude of the horizontal buoyancy gradient ($|\nabla_h b|^2$), as they are identical:

$$\partial_n b \equiv \frac{\nabla_h \rho}{|\nabla_h \rho|} \cdot \nabla_h b = \frac{\nabla_h \rho}{|\nabla_h \rho|} \cdot \left(-\frac{g}{\rho_0} \nabla_h \rho\right) = -\frac{g}{\rho_0} \left|\nabla_h \rho\right| = -\left|\nabla_h b\right|. \tag{28}$$

Finally, we substitute the horizontal buoyancy gradient $\overline{\nabla_h b}^z$ by observable submesoscale SSH gradient ($\nabla_h \eta_{\mathrm{submeso}}$) or the ML steric height gradient ($\nabla_h \eta_{\mathrm{steric}}$), using Eq. 9 ($\langle H \rangle \overline{\nabla_h b}^z \approx g \nabla_h \eta_{\mathrm{steric}}$) and Eq. 12 ($\nabla_h \eta_{\mathrm{submeso}} \approx \nabla_h \eta_{\mathrm{steric}}$):

$$\begin{aligned} \left\langle \mathrm{VHF_{MLE}} \right\rangle &\approx \frac{\rho_0 C_p C_e \mu_0 g}{\alpha |f|} \left\langle \left| \nabla_h \eta_{\mathrm{steric}} \right|^2 r^s \right\rangle \\ &\approx \frac{\rho_0 C_p C_e \mu_0 g}{\alpha |f|} \left\langle \left| \nabla_h \eta_{\mathrm{submeso}} \right|^2 r^s \right\rangle, \end{aligned} \tag{29}$$

As the magnitude of the thermal expansion coefficient α depends on temperature, it shows strong seasonal variability (Fig. S6a). We choose an annual-mean value of $\alpha = 1.60 \times 10^{-4}\,^{\circ}\mathrm{C}^{-1}$. While different choices of α modify the magnitude of the theoretical prediction, the results shown in Fig. 3(c) remain robust (Fig. S7).

In principle, Eqs. 27-29 are applicable only in regions and seasons where the horizontal and vertical Turner angles show good agreement. This requirement arises because a close alignment between Tu_v and Tu_h is necessary for using the surface buoyancy ratio r^s as a proxy for the mean buoyancy ratio throughout the ML (Eqs. 25, 27). Nevertheless, the theory performs well throughout the year (Fig. 3c), likely because the summertime eddy VBF is too small to produce noticeable errors. Note that temperature–salinity compensation (Spiro Jaeger & Mahadevan, 2018) does not affect our results, as it is implicitly included in the buoyancy ratio r.

6 Conclusion and discussions

In this study, we proposed a theoretical framework to estimate vertical buoyancy and heat fluxes, as well as to reconstruct the evolution of MLD from the sea surface state. The gradient magnitude and Laplacian of the ML steric height closely match the spatially filtered SSH anomaly, revealing clear surface imprints of the mixed layer eddies and fronts. This enables us to parameterize the ML eddy-induced vertical buoyancy and heat fluxes using submesoscale SSH. Based on the parameterized eddy buoyancy flux, we developed a theory to reconstruct changes in the MLD from surface variables. The theoretical reconstruction of the MLD agree well with model diagnostics during periods with

pronounced submesoscale activity. Despite being conducted in different regions and seasons, our estimates of submesoscale vertical fluxes agree well with recent airborne observations by Torres et al. (2025), which show that submesoscale processes contribute more than 80% of the vertical heat flux, with values reaching $227\,\mathrm{W/m^2}$. Our vertical heat flux estimates also agrees quantitatively with those of Su et al. (2018).

Although the theory performs well, several caveats highlight avenues for further research. Our theory builds on the parameterization of Fox-Kemper et al. (2008), which does not account for the effects of wind (Mahadevan et al., 2010) or boundary layer turbulence (Bodner et al., 2023) on submesoscale fronts. Because the model lacks coupled air–sea dynamics, the Ekman buoyancy flux may be underestimated in this study. In addition, vertical mixing in LLC4320 is parameterized using the K-Profile Parameterization (Large et al., 1994), which can contribute to anomalously deep mixed layers in regions of strong open-ocean convection (Sohail et al., 2020), such as the Icelandic Basin (Text S6, Fig. S8). Moreover, the MLD budget does not include horizontal advection through lateral boundaries and turbulent mixing at the base of the ML, which may play important roles in regions with strong boundary currents and wave breaking. Notably, horizontal advection could potentially be incorporated into this framework by estimating it from the SSH gradient under the assumption of geostrophic balance.

Our method provides a framework for diagnosing subsurface dynamics from surface observations, providing a physically-grounded approach complimentary to the machine-learning-based inference from SWOT SSH anomalies proposed by Champenois et al. (2026). Given satellite observations of SSH, surface temperature, salinity, and surface heat flux, this approach permits an estimate of ML-averaged vertical heat flux and the tendency of the MLD. Using MLD observations from *in-situ* measurements such as Argo floats as initial conditions, the MLD can be reconstructed over several months at resolutions higher than the standard gridded products. It should be noted that our theory is applicable only during seasons with pronounced ML eddy activity. In addition, the theory is intended for horizontally averaged quantities; applying it at individual points can lead to deviations. The present analysis focuses on springtime restratification, and future work will be needed to evaluate the theory across different forcing regimes.

Data and Code Availability

The code and data used in this manuscript are available at https://github.com/bodner-research-group/surface_submesoscale. The bathymetric data used in Fig. 1(a) comes from ETOPO (2022).

Conflict of Interest declaration

The authors declare there are no conflicts of interest for this manuscript.

Acknowledgments

This work was supported by NASA award number 80NSSC24K1664. We acknowledge the MIT Office of Research Computing and Data for providing high performance computing and data storage resources. We thank Dimitris Menemenlis and Hector Torres for making LLC4320 model output available. We sincerely appreciate Tatsu Monkman for helpful guidance on accessing the LLC4320 dataset. We also thank Jinbo Wang, Spencer Jones, Dhruv Balwada, and Shafer Smith for valuable discussions.

References

Archer, M., Wang, J., Klein, P., Dibarboure, G., & Fu, L.-L. (2025). Wide-swath satellite altimetry unveils global submesoscale ocean dynamics. *Na-*

ture, *640*(8059), 691–696. Retrieved from https://doi.org/10.1038/s41586-025-08722-8

Balwada, D., Xiao, Q., Smith, S., Abernathey, R., & Gray, A. R. (2021). Vertical fluxes conditioned on vorticity and strain reveal submesoscale ventilation. *Journal of Physical Oceanography*, *51*(9), 2883–2901. Retrieved from https://doi.org/10.1175/JPO-D-21-0016.1

Biddle, L., & Swart, S. (2020). The observed seasonal cycle of submesoscale processes in the Antarctic marginal ice zone. *Journal of Geophysical Research: Oceans*, *125*(6), e2019JC015587. Retrieved from https://doi.org/10.1029/2019JC015587

Boccaletti, G., Ferrari, R., & Fox-Kemper, B. (2007). Mixed layer instabilities and restratification. *Journal of Physical Oceanography*, *37*(9), 2228–2250. Retrieved from https://doi.org/10.1175/JPO3101.1

Bodner, A. S., Fox-Kemper, B., Johnson, L., Van Roekel, L. P., McWilliams, J. C., Sullivan, P. P., ... Dong, J. (2023). Modifying the mixed layer eddy parameterization to include frontogenesis arrest by boundary layer turbulence. *Journal of Physical Oceanography*, *53*(1), 323–339. Retrieved from https://doi.org/10.1175/JPO-D-21-0297.1

Buckingham, C. E., Lucas, N. S., Belcher, S. E., Rippeth, T. P., Grant, A. L., Le Sommer, J., ... Naveira Garabato, A. C. (2019). The contribution of surface and submesoscale processes to turbulence in the open ocean surface boundary layer. *Journal of Advances in Modeling Earth Systems*, *11*(12), 4066–4094. Retrieved from https://doi.org/10.1029/2019MS001801

Carli, E., Siegelman, L., Morrow, R., & Vergara, O. (2024). Surface quasi geostrophic reconstruction of vertical velocities and vertical heat fluxes in the Southern Ocean: Perspectives for SWOT. *Journal of Geophysical Research: Oceans*, *129*(9), e2024JC021216. Retrieved from https://doi.org/10.1029/2024JC021216

Champenois, B., Ali, A., & Bodner, A. (2026). Reconstructing ocean mixed layer variability from SWOT using machine learning. *Authorea Preprints*. Retrieved from https://doi.org/10.22541/essoar.177046572.22898014/v1

de Boyer Montégut, C., Madec, G., Fischer, A. S., Lazar, A., & Iudicone, D. (2004). Mixed layer depth over the global ocean: An examination of profile data and a profile-based climatology. *Journal of Geophysical Research: Oceans*, *109*(C12). Retrieved from https://doi.org/10.1029/2004JC002378

Delman, A. (2025, August). *Part 3: Steric height.* Retrieved from https://ecco-v4-python-tutorial.readthedocs.io/Steric_height.html (ECCO Version 4 Python Tutorial)

Dong, J., Fox-Kemper, B., Zhang, H., & Dong, C. (2020). The scale of submesoscale baroclinic instability globally. *Journal of Physical Oceanography*, *50*(9), 2649–2667. Retrieved from https://doi.org/10.1175/JPO-D-20-0043.1

Dù, R. S., Smith, K. S., & Bühler, O. (2025). Next-order balanced model captures submesoscale physics and statistics. *Journal of Physical Oceanography*, *55*(10), 1679–1697. Retrieved from https://doi.org/10.1175/JPO-D-24-0146.1

Fox-Kemper, B., & Ferrari, R. (2008). Parameterization of mixed layer eddies. Part II: Prognosis and impact. *Journal of Physical Oceanography*, *38*(6), 1166–1179. Retrieved from https://doi.org/10.1175/2007JPO3788.1

Fox-Kemper, B., Ferrari, R., & Hallberg, R. (2008). Parameterization of mixed layer eddies. Part I: Theory and diagnosis. *Journal of Physical Oceanography*, *38*(6), 1145–1165. Retrieved from https://doi.org/10.1175/2007JPO3792.1

Gallmeier, K., Prochaska, J. X., Cornillon, P., Menemenlis, D., & Kelm, M. (2023). An evaluation of the LLC4320 global-ocean simulation based on the submesoscale structure of modeled sea surface temperature fields. *Geoscientific Model Development*, *16*(23), 7143–7170. Retrieved from https://doi.org/10.5194/gmd-16-7143-2023

Guo, M., Xing, X., Xiu, P., Dall'Olmo, G., Chen, W., & Chai, F. (2024). Efficient biological carbon export to the mesopelagic ocean induced by submesoscale fronts. *Nature Communications*, *15*(1), 580. Retrieved from https://doi.org/10.1038/s41467-024-44846-7

Johnson, L., Fox-Kemper, B., Li, Q., Pham, H. T., & Sarkar, S. (2023). A finite-time ensemble method for mixed layer model comparison. *Journal of Physical Oceanography*, *53*(9), 2211–2230. Retrieved from https://doi.org/10.1175/JPO-D-22-0107.1

Johnson, L., Lee, C. M., & D'Asaro, E. A. (2016). Global estimates of lateral springtime restratification. *Journal of Physical Oceanography*, *46*(5), 1555–1573. Retrieved from https://doi.org/10.1175/JPO-D-15-0163.1

Johnson, L., Lee, C. M., D'Asaro, E. A., Thomas, L., & Shcherbina, A. (2020). Restratification at a California current upwelling front. Part I: Observations. *Journal of Physical Oceanography*, *50*(5), 1455–1472. Retrieved from https://doi.org/10.1175/JPO-D-19-0203.1

Khatri, H., Griffies, S. M., Uchida, T., Wang, H., & Menemenlis, D. (2021). Role of mixed-layer instabilities in the seasonal evolution of eddy kinetic energy spectra in a global submesoscale permitting simulation. *Geophysical Research Letters*, *48*(18), e2021GL094777. Retrieved from https://doi.org/10.1029/2021GL094777

Kraus, E., & Turner, J. (1967). A one-dimensional model of the seasonal thermocline II. The general theory and its consequences. *Tellus*, *19*(1), 98–106. Retrieved from https://doi.org/10.3402/tellusa.v19i1.9753

Large, W. G., McWilliams, J. C., & Doney, S. C. (1994). Oceanic vertical mixing: A review and a model with a nonlocal boundary layer parameterization. *Reviews of geophysics*, *32*(4), 363–403. Retrieved from https://doi.org/10.1029/94RG01872

Mahadevan, A. (2016). The impact of submesoscale physics on primary productivity of plankton. *Annual review of marine science*, *8*(1), 161–184. Retrieved from https://doi.org/10.1146/annurev-marine-010814-015912

Mahadevan, A., D'asaro, E., Lee, C., & Perry, M. J. (2012). Eddy-driven stratification initiates North Atlantic spring phytoplankton blooms. *science*, *337*(6090), 54–58. Retrieved from https://doi.org/10.1126/science.1218740

Mahadevan, A., Tandon, A., & Ferrari, R. (2010). Rapid changes in mixed layer stratification driven by submesoscale instabilities and winds. *Journal of Geophysical Research: Oceans*, *115*(C3). Retrieved from https://doi.org/10.1029/2008JC005203

Marshall, J., Adcroft, A., Hill, C., Perelman, L., & Heisey, C. (1997). A finite-volume, incompressible Navier Stokes model for studies of the ocean on parallel computers. *J. Geophys. Res.*, *102*, 5753–5766. Retrieved from https://doi.org/10.1029/96JC02775

Marshall, J., Hill, C., Perelman, L., & Adcroft, A. (1997). Hydrostatic, quasi-hydrostatic, and nonhydrostatic ocean modeling. *J. Geophys. Res.*, *102*, 5733–5752. Retrieved from https://doi.org/10.1029/96JC02776

Marshall, J., & Schott, F. (1999). Open-ocean convection: Observations, theory, and models. *Reviews of geophysics*, *37*(1), 1–64. Retrieved from https://doi.org/10.1029/98RG02739

McWilliams, J. C. (2019). A survey of submesoscale currents. *Geoscience Letters*, *6*(1), 3. Retrieved from https://doi.org/10.1186/s40562-019-0133-3

NOAA National Centers for Environmental Information. (2022). *ETOPO 2022 15 Arc-Second Global Relief Model.* Retrieved from https://doi.org/10.25921/fd45-gt74

Siegelman, L. (2020). Energetic submesoscale dynamics in the ocean interior. *Journal of Physical Oceanography*, *50*(3), 727–749. Retrieved from https://doi.org/10.1175/JPO-D-19-0253.1

Siegelman, L., Klein, P., Rivière, P., Thompson, A. F., Torres, H. S., Flexas, M., & Menemenlis, D. (2020). Enhanced upward heat transport at deep submesoscale ocean fronts. *Nature Geoscience*, *13*(1), 50–55. Retrieved from https://doi.org/10.1038/s41561-019-0489-1

Sohail, T., Gayen, B., & McC. Hogg, A. (2020). The dynamics of mixed layer deepening during open-ocean convection. *Journal of Physical Oceanography*, *50*(6), 1625–1641. Retrieved from https://doi.org/10.1175/JPO-D-19-0264.1

Spiro Jaeger, G., & Mahadevan, A. (2018). Submesoscale-selective compensation of fronts in a salinity-stratified ocean. *Science advances*, *4*(2), e1701504. Retrieved from https://doi.org/10.1126/sciadv.1701504

Spungin, S., Si, Y., Stewart, A. L., & Prend, C. J. (2025). Observed seasonality of mixed-layer eddies and vertical heat transport over the Antarctic continental shelf. *Journal of Geophysical Research: Oceans*, *130*(3), e2024JC021564. Retrieved from https://doi.org/10.1029/2024JC021564

Srinivasan, K., Barkan, R., & McWilliams, J. C. (2023). A forward energy flux at submesoscales driven by frontogenesis. *Journal of Physical Oceanography*, *53*(1), 287–305. Retrieved from https://doi.org/10.1175/JPO-D-22-0001.1

Stone, P. H. (1970). On non-geostrophic baroclinic stability: Part ii. *Journal of Atmospheric Sciences*, *27*(5), 721–726. Retrieved from https://doi.org/10.1175/1520-0469(1970)027%3C0721:ONGBSP%3E2.0.CO;2

Su, Z., Wang, J., Klein, P., Thompson, A. F., & Menemenlis, D. (2018). Ocean submesoscales as a key component of the global heat budget. *Nature communications*, *9*(1), 775. Retrieved from https://doi.org/10.1038/s41467-018-02983-w

Taylor, J. R., & Thompson, A. F. (2023). Submesoscale dynamics in the upper ocean. *Annual Review of Fluid Mechanics*, *55*(1), 103–127. Retrieved from https://doi.org/10.1146/annurev-fluid-031422-095147

Thomas, L., & Ferrari, R. (2008). Friction, frontogenesis, and the stratification of the surface mixed layer. *Journal of Physical Oceanography*, *38*(11), 2501–2518. Retrieved from https://doi.org/10.1175/2008JPO3797.1

Thomas, L., & Lee, C. M. (2005). Intensification of ocean fronts by down-front winds. *Journal of Physical Oceanography*, *35*(6), 1086–1102. Retrieved from https://doi.org/10.1175/JPO2737.1

Thomas, L., Taylor, J. R., Ferrari, R., & Joyce, T. M. (2013). Symmetric instability in the Gulf Stream. *Deep Sea Research Part II: Topical Studies in Oceanography*, *91*, 96–110. Retrieved from https://doi.org/10.1016/j.dsr2.2013.02.025

Thompson, A. F., Lazar, A., Buckingham, C., Naveira Garabato, A. C., Damerell, G. M., & Heywood, K. J. (2016). Open-ocean submesoscale motions: A full seasonal cycle of mixed layer instabilities from gliders. *Journal of Physical Oceanography*, *46*(4), 1285–1307. Retrieved from https://doi.org/10.1175/JPO-D-15-0170.1

Torres, H. S., Wineteer, A., Rodriguez, E., Klein, P., Thompson, A. F., Perkovic-Martin, D., ... others (2025). Submesoscale eddy contribution to ocean vertical heat flux diagnosed from airborne observations. *Geophysical Research Letters*, *52*(2), e2024GL112278. Retrieved from https://doi.org/10.1029/2024GL112278

Treguier, A. M., de Boyer Montégut, C., Bozec, A., Chassignet, E. P., Fox-Kemper, B., McC. Hogg, A., ... others (2023). The mixed-layer depth in the ocean model intercomparison project (omip): impact of resolving mesoscale eddies. *Geoscientific Model Development*, *16*(13), 3849–3872. Retrieved from https://doi.org/10.5194/gmd-16-3849-2023

Uchida, T., Le Sommer, J., Stern, C., Abernathey, R., Holdgraf, C., Albert, A., ... others (2022). Cloud-based framework for inter-comparing submesoscale

permitting realistic ocean models. *Geoscientific Model Development*, *15*, 5829–5856. Retrieved from https://doi.org/10.5194/gmd-15-5829-2022

Wang, J., Lucas, A. J., Stalin, S., Lankhorst, M., Send, U., Schofield, O., ... others (2025). SWOT mission validation of sea surface height measurements at sub-100 km scales. *Geophysical Research Letters*, *52*(11), e2025GL114936. Retrieved from https://doi.org/10.1029/2025GL114936

Wenegrat, J. O. (2023). The current feedback on stress modifies the Ekman buoyancy flux at fronts. *Journal of Physical Oceanography*, *53*(12), 2737–2749. Retrieved from https://doi.org/10.1175/JPO-D-23-0005.1

Yu, X., Barkan, R., & Naveira Garabato, A. C. (2024). Intensification of submesoscale frontogenesis and forward energy cascade driven by upper-ocean convergent flows. *Nature Communications*, *15*(1), 9214. Retrieved from https://doi.org/10.1038/s41467-024-53551-4

Zhang, X., & Callies, J. (2025). Assessing submesoscale sea surface height signals from the swot mission. *Journal of Geophysical Research: Oceans*, *130*(10), e2025JC022879. Retrieved from https://doi.org/10.1029/2025JC022879

Zhang, Y., Zhang, S., & Afanasyev, Y. (2025). Energy cascades in surface semi-geostrophic turbulence: Implications for the oceanic submesoscale flows. *Journal of Geophysical Research: Oceans*, *130*(2), e2023JC020868. Retrieved from https://doi.org/10.1029/2023JC020868

Zhang, Z., Chang, J., Zhang, X., & Zhang, W. (2025). Mixed transitional layer instability: A mechanism for deep-penetrating submesoscale processes in the subtropical upper ocean. *Journal of Physical Oceanography*, *55*(12), 2269–2283. Retrieved from https://doi.org/10.1175/JPO-D-25-0009.1

Zhang, Z., Miao, M., Qiu, B., Tian, J., Jing, Z., Chen, G., ... Zhao, W. (2024). Submesoscale eddies detected by swot and moored observations in the northwestern pacific. *Geophysical Research Letters*, *51*(15), e2024GL110000. Retrieved from https://doi.org/10.1029/2024GL110000

Supporting Information for "Uncovering Ocean Mixed Layer Dynamics from the Sea Surface State"

Yidongfang Si[1], Leah Johnson[2], and Abigail Bodner[1,3]

[1]Department of Earth, Atmospheric and Planetary Sciences, Massachusetts Institute of Technology, Cambridge, MA

[2]Applied Physics Laboratory, University of Washington, Seattle, WA

[3]Department of Electrical Engineering and Computer Science, Massachusetts Institute of Technology, Cambridge, MA

Contents of this file

Text S1. Mixed-layer steric height

In the main manuscript, we define the mixed-layer steric height as the *in situ* density anomaly integrated vertically from the domain-averaged mixed-layer base, $-\langle H \rangle$, to the sea surface (Eq. 7). The discrepancies between the mixed-layer steric height and submesoscale SSH shown in Fig. 2b–c result from this definition, as the mixed layer depth varies substantially within the selected domain.

If instead the integration is performed from the local mixed layer depth, $H(x, y, t)$, *i.e.*,

$$\eta_{\text{steric}} = -\frac{1}{\rho_0} \int_{-H}^{0} \rho'_{\text{in situ}} dz,$$

in Eq. 9, the Leibniz integral rule must be applied when computing the horizontal gradient of η_{steric} to account for spatial variations in the mixed layer depth:

$$\nabla_h \eta_{\text{steric}} = -\frac{1}{\rho_0} \int_{-H}^{0} \nabla_h \rho'_{\text{in situ}} dz - \frac{1}{\rho_0} \rho'_{\text{in situ}} \Big|_{z=-H} \nabla_h H.$$

The last term may complicate the mixed-layer eddy parameterizations based on steric height and submesoscale SSH, although it is likely small because $\nabla_h \eta_{\text{steric}}$ in the equation above is primarily controlled by local horizontal density gradients rather than by large-scale variations in the mixed layer depth.

Text S2. Seasonality of the most unstable mixed layer instability wavelength

In the Icelandic Basin, the wavelength of the most unstable mixed-layer instability mode λ_{MLI} peaks in winter and early spring, and reaches its seasonal minimum during summer (Fig. S2a). This seasonal cycle can be understood as follows:

Given the definition of the mixed layer depth in Eq. 5 of the main text ($\overline{N^2}^z = g\Delta\rho/(\rho_0 H)$), λ_{MLI} can be approximated as

$$\begin{aligned}
\lambda_{\mathrm{MLI}} &= \frac{2\pi}{\sqrt{5/2}} L_d \sqrt{1 + Ri_b^{-1}} \\
&= \frac{2\pi}{\sqrt{5/2}} \frac{\overline{N}^z H}{f} \sqrt{1 + \left(\overline{N^2 f^2 / |\nabla_h b|^2}^{\mathrm{hm},\, z} \right)^{-1}} \\
&\approx \frac{2\pi}{\sqrt{5/2} f} \sqrt{\overline{N^2}^z H^2 + \frac{\overline{|\nabla_h b|^2}^z}{f^2} H^2} \\
&= \frac{2\pi}{\sqrt{5/2} f} \sqrt{\frac{g\Delta\rho}{\rho_0} H + \frac{\overline{|\nabla_h b|^2}^z}{f^2} H^2}
\end{aligned}$$

indicating that it is largely controlled by the mixed layer depth H (Fig. S2).

Text S3. Sensitivity of submesoscale SSH to filter size

In the main manuscript we adopt a time-dependent filter for submesoscale SSH (Eq. 11) to account for the seasonal variability in eddy size. Here, we test the sensitivity of submesoscale SSH to the choice of filter size. We reproduce Figs. 2(j), 3(b), and 3(c) of the main manuscript using a constant Gaussian filter instead of the time-varying filter, with the filter size (Gaussian full width at half maximum) set to 17 km.

From January to late March, when the horizontal and vertical Turner angles agree well, the theory reliably reconstructs the mixed layer depth and vertical heat flux with a constant filter (Fig. S3). This suggests that during periods with strong submesoscale activity, the method is relatively insensitive to the choice of filter.

From April to September, the constant filter size exceeds the most unstable mixed layer instability wavelength. As a result, the gradient magnitude of submesoscale SSH is overestimated (Fig. S3a), leading to overestimation of the eddy-induced vertical heat

flux (Fig. S3c) and excessively rapid shoaling of the reconstructed mixed layer depth (Fig. S3b).

Text S4. Ekman buoyancy flux

In principle, the horizontal buoyancy gradient averaged over the Ekman layer should be used to estimate the Ekman buoyancy flux. However, because the Ekman layer depth cannot be diagnosed without the knowledge of the vertical eddy viscosity in the K-profile parameterization (KPP), we instead use the surface buoyancy gradient as an approximation in Section 4.3 of the main manuscript. This approximation has been widely used in previous studies (*e.g.*, Zheng et al., 2025; Wenegrat, 2023).

Text S5. Eddy-induced vertical buoyancy flux

In Section 4.4 of the main manuscript, we define the eddy-induced vertical buoyancy flux (VBF) as

$$B_{\text{eddy}} = -\overline{w'b'}^{z} \equiv -\overline{(w-\tilde{w})(b-\tilde{b})}^{z}. \tag{1}$$

Here, we used a Gaussian filter with a standard deviation of 30 km, which is larger than the filter applied to the submesoscale SSH. We find that the selected filter scales provide the best agreement with eddy baroclinic instabilities.

Zhang et al. (2025) show that in LLC4320, energy injection in the mixed layer occurs at scales larger than λ_{MLI}, the most unstable wavelength of mixed-layer instability (their Figs. 4–5), arising from mixed-layer instability, transitional-layer instability, or mesoscale eddies. This is consistent with our finding that the filter scale needs to be slightly larger for the eddy buoyancy flux to account for these additional affects.

Increasing the filter scale incorporates contributions from mesoscale processes, with mesoscale eddies (horizontal scales ranging from 30 km to 60 km) contributing about 13% of the total vertical buoyancy flux (Fig. S5), while scales smaller than 30 km contributing about 87%. This agrees with the airborne observations by Torres et al. (2025), which show that submesoscale processes contribute more than 80% of the vertical heat flux.

Additionally, although the Gaussian filter does not preserve the Reynolds decomposition required for exact buoyancy budget closure, it is adequate for this leading-order analysis, and replacing it with a box filter (horizontal coarse graining) that preserves the Reynolds decomposition yields very similar results.

Text S6. KPP boundary layer depth

In LLC4320, the boundary layer depth in the K-Profile Parameterization (KPP) is defined as the shallowest depth at which the Richardson number reaches a critical threshold of $Ri_c = 0.3559$. The deep KPP boundary layer observed during winter appears to be associated with open-ocean convection driven by strong surface cooling. Large spikes in the KPP boundary layer depth (Fig. S8a) are likely associated with abrupt changes in surface wind stress (Fig. S8b).

The mismatch between the KPP boundary layer depth and the mixed layer depth (pink shading in Fig. S8a) during spring may indicate the presence of springtime eddy restratification, coinciding with the period of good Turner angle agreement (Fig. 1b).

References

Torres, H. S., Wineteer, A., Rodriguez, E., Klein, P., Thompson, A. F., Perkovic-Martin,

D., ... others (2025). Submesoscale eddy contribution to ocean vertical heat flux diagnosed from airborne observations. *Geophysical Research Letters*, *52*(2), e2024GL112278. Retrieved from https://doi.org/10.1029/2024GL112278

Wenegrat, J. O. (2023). The current feedback on stress modifies the Ekman buoyancy flux at fronts. *Journal of Physical Oceanography*, *53*(12), 2737–2749. Retrieved from https://doi.org/10.1175/JPO-D-23-0005.1

Zhang, Z., Chang, J., Zhang, X., & Zhang, W. (2025). Mixed transitional layer instability: A mechanism for deep-penetrating submesoscale processes in the subtropical upper ocean. *Journal of Physical Oceanography*, *55*(12), 2269–2283. Retrieved from https://doi.org/10.1175/JPO-D-25-0009.1

Zheng, Z., Wenegrat, J. O., Fox-Kemper, B., & Brett, G. J. (2025). Wind-Catalyzed Energy Exchanges between Fronts and Boundary Layer Turbulence. *Journal of Physical Oceanography*, *55*(9), 1591–1606. Retrieved from https://doi.org/10.1175/JPO-D-24-0243.1

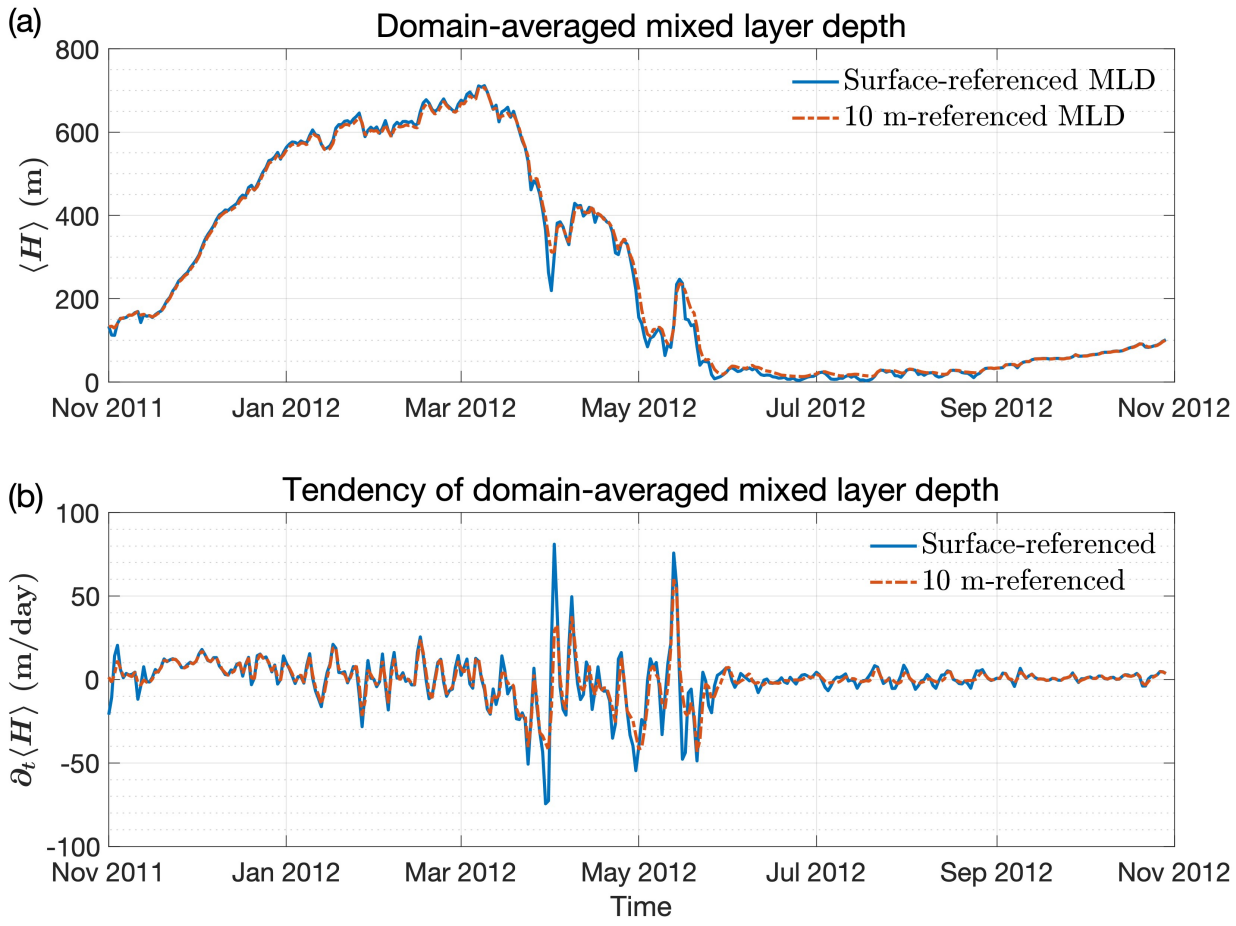

Figure S1. Sensitivity of mixed layer depth to the reference depth. Time series of the daily- and domain-averaged mixed layer depth, $\langle H \rangle$ (a), and its time derivative, $\partial_t \langle H \rangle$ (b). The red curves show the mixed layer depth defined relative to a 10-m reference depth, while the blue curves show the mixed layer depth defined relative to the ocean surface.

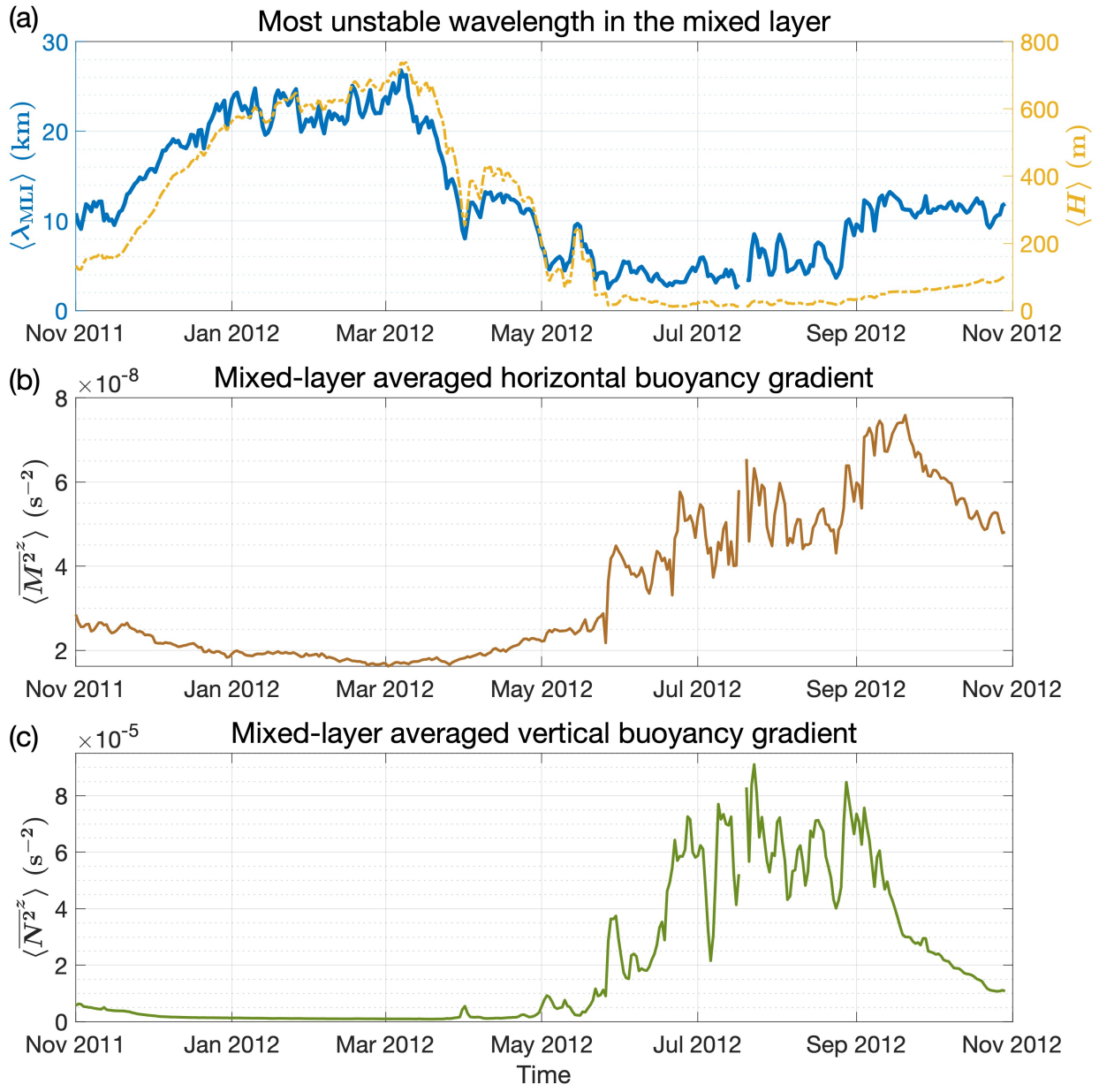

Figure S2. Time series of the domain-averaged (a) wavelength of the most unstable mixed-layer instability mode (blue) and surface-referenced mixed layer depth (yellow), (b) mixed-layer averaged horizontal buoyancy gradient, and (c) mixed-layer averaged vertical buoyancy gradient.

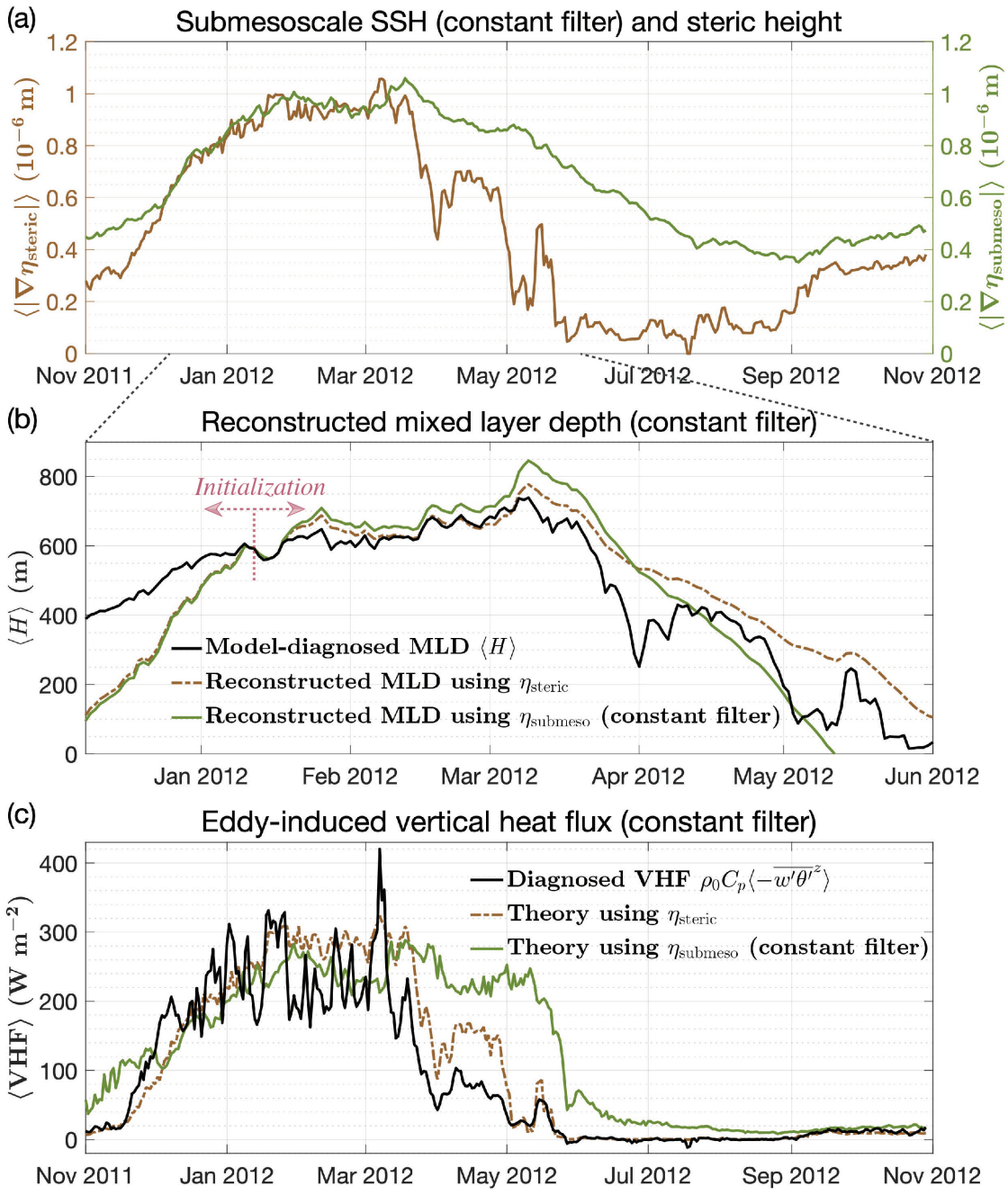

Figure S3. Similar to Figs. 2(j), 3(b), and 3(c) of the main manuscript, but using a constant Gaussian filter instead of a time-varying filter based on the time series of the most unstable mixed-layer instability wavelength. The submesoscale SSH is computed with a fixed filter size of 17 km. (a) Time series of the gradient magnitude of submesoscale SSH computed with the constant filter (green) and steric height (brown). (b) Reconstructed mixed-layer depth. (c) Eddy-induced vertical heat flux.

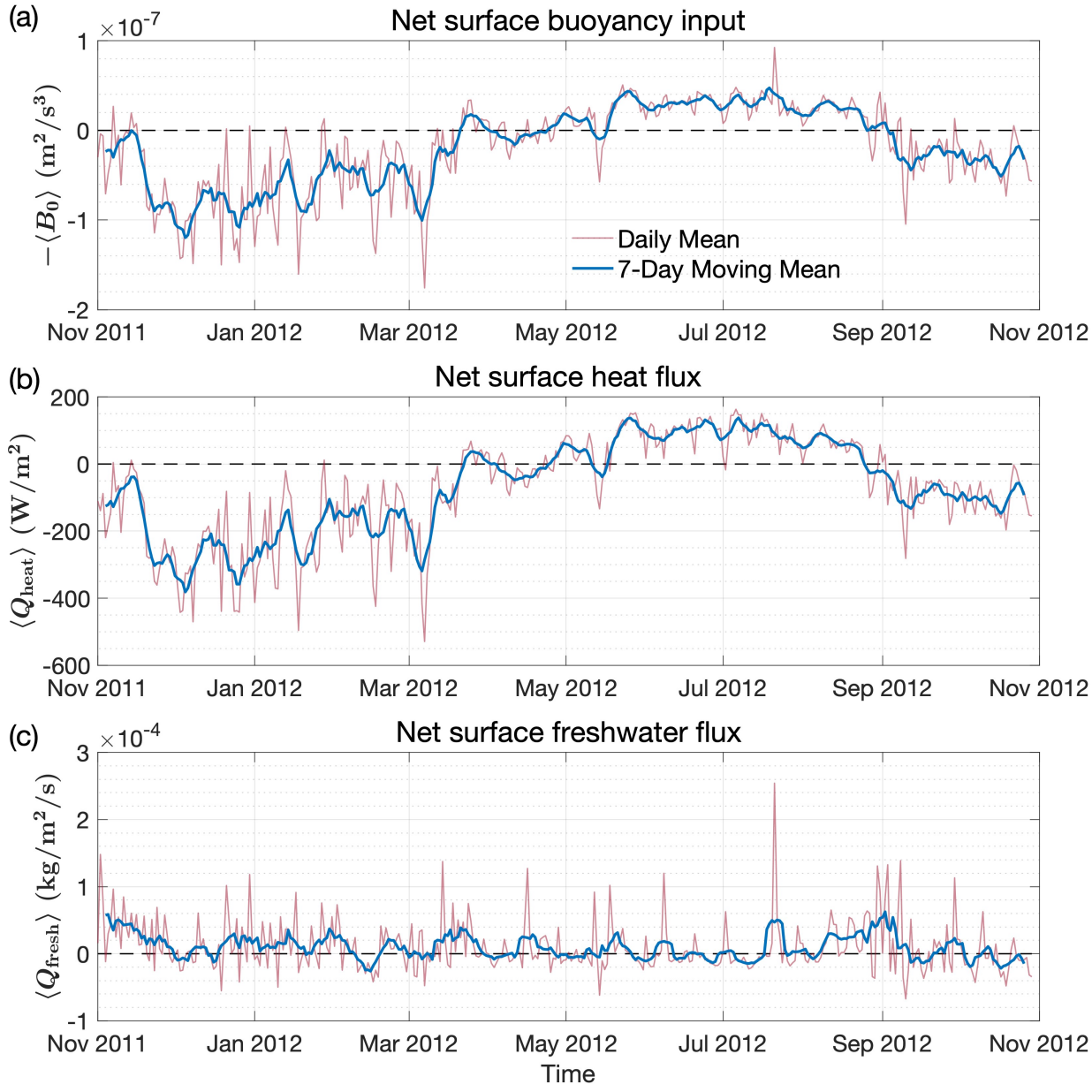

Figure S4. Time series of the domain-averaged net surface (a) buoyancy input ($-\langle B_0 \rangle$), (b) heat flux ($\langle Q_{\text{heat}} \rangle$), and (c) fresh water flux ($\langle Q_{\text{fresh}} \rangle$).

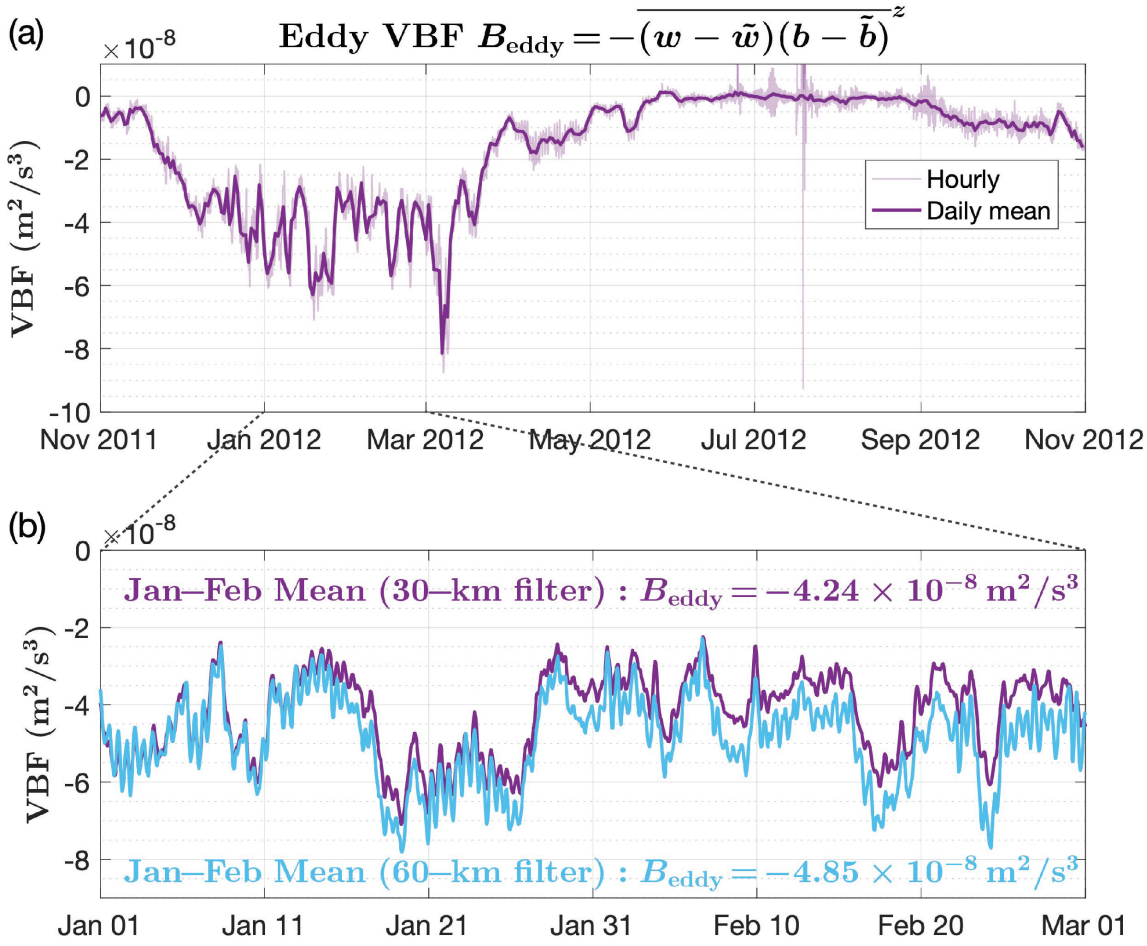

Figure S5. Time series of the eddy-induced vertical buoyancy flux (VBF) over the full year (panel a: hourly and daily) and for January 1–March 1, 2012 (panel b: hourly). The Gaussian filter has a standard deviation of 30 km for the purple curves and 60 km for the blue curve.

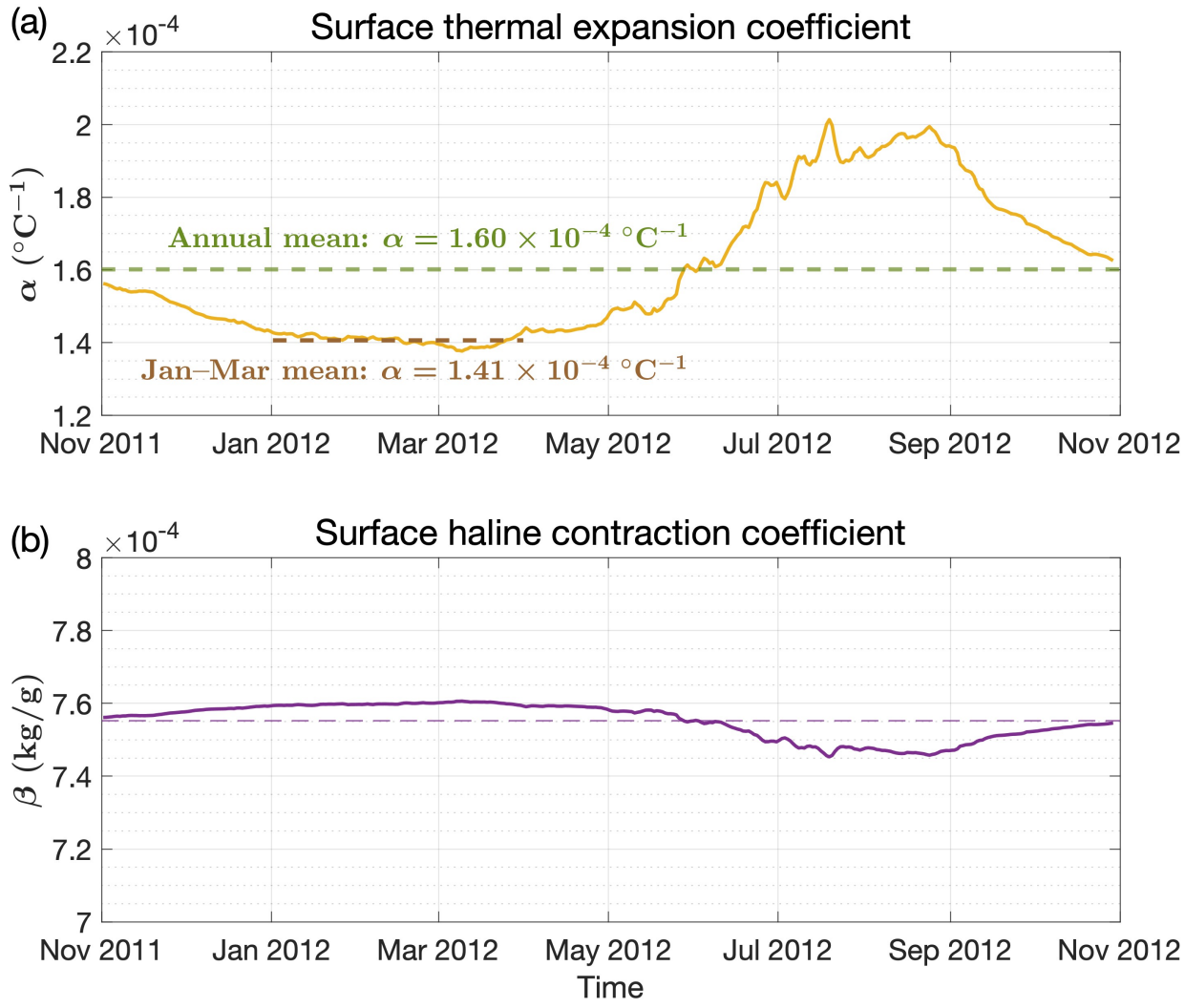

Figure S6. Surface thermal expansion coefficient (a) and haline contraction coefficient (b), averaged daily and over the domain. The dashed lines denote the mean values.

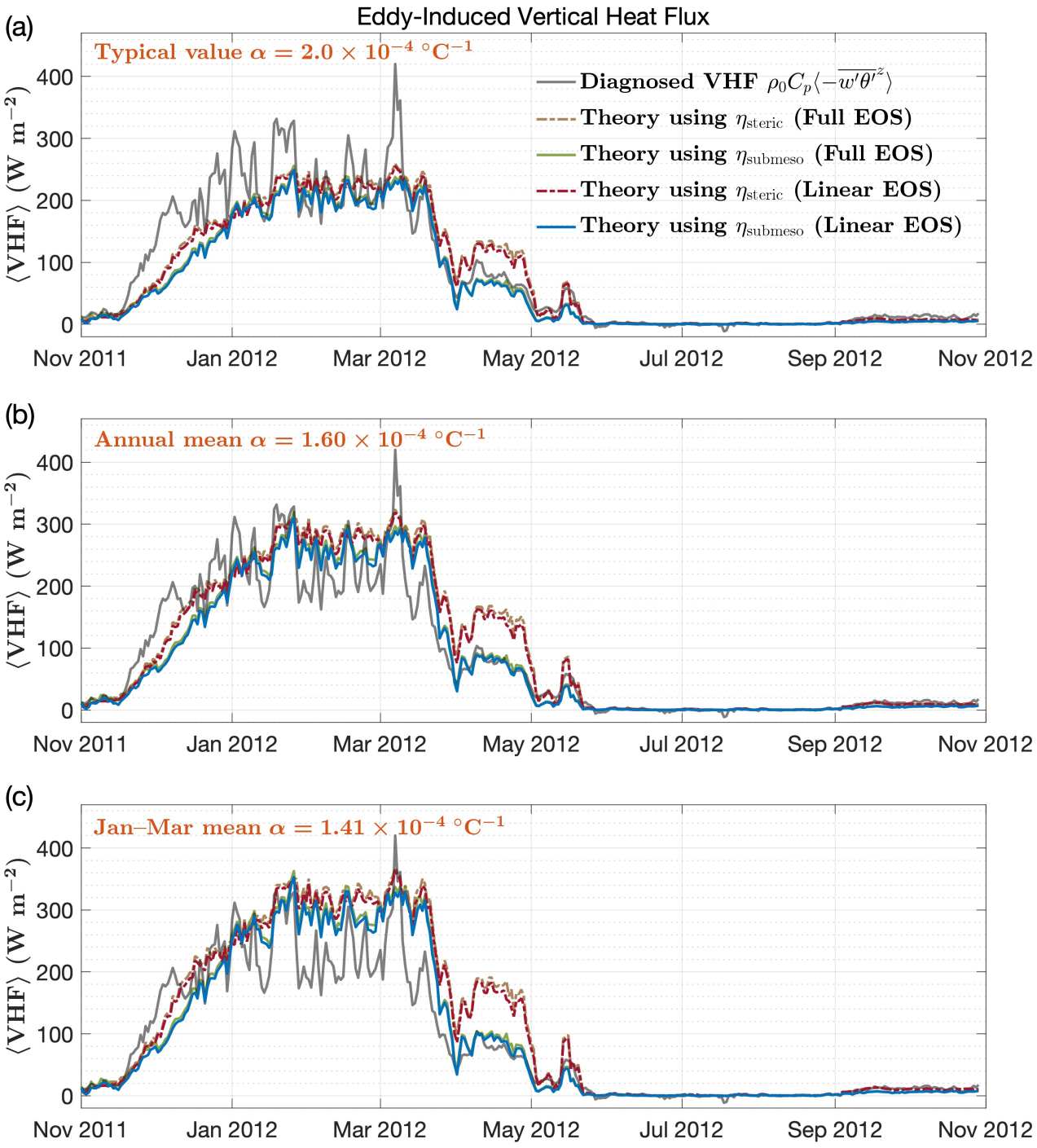

Figure S7. Time series of diagnosed VHF and theoretical estimates using η_{steric} (dash–dot) and η_{submeso} (solid), computed with the full equation of state (EOS) (brown, green) and a linear EOS (red, blue). (a) Using a typical value for the thermal expansion coefficient, $\alpha = 2.0 \times 10^{-4}$ °C^{-1}. (b) Using the annual-mean value of $\alpha = 1.60 \times 10^{-4}$ °C^{-1}. (c) Using the Jan–Mar mean $\alpha = 1.41 \times 10^{-4}$ °C^{-1}.

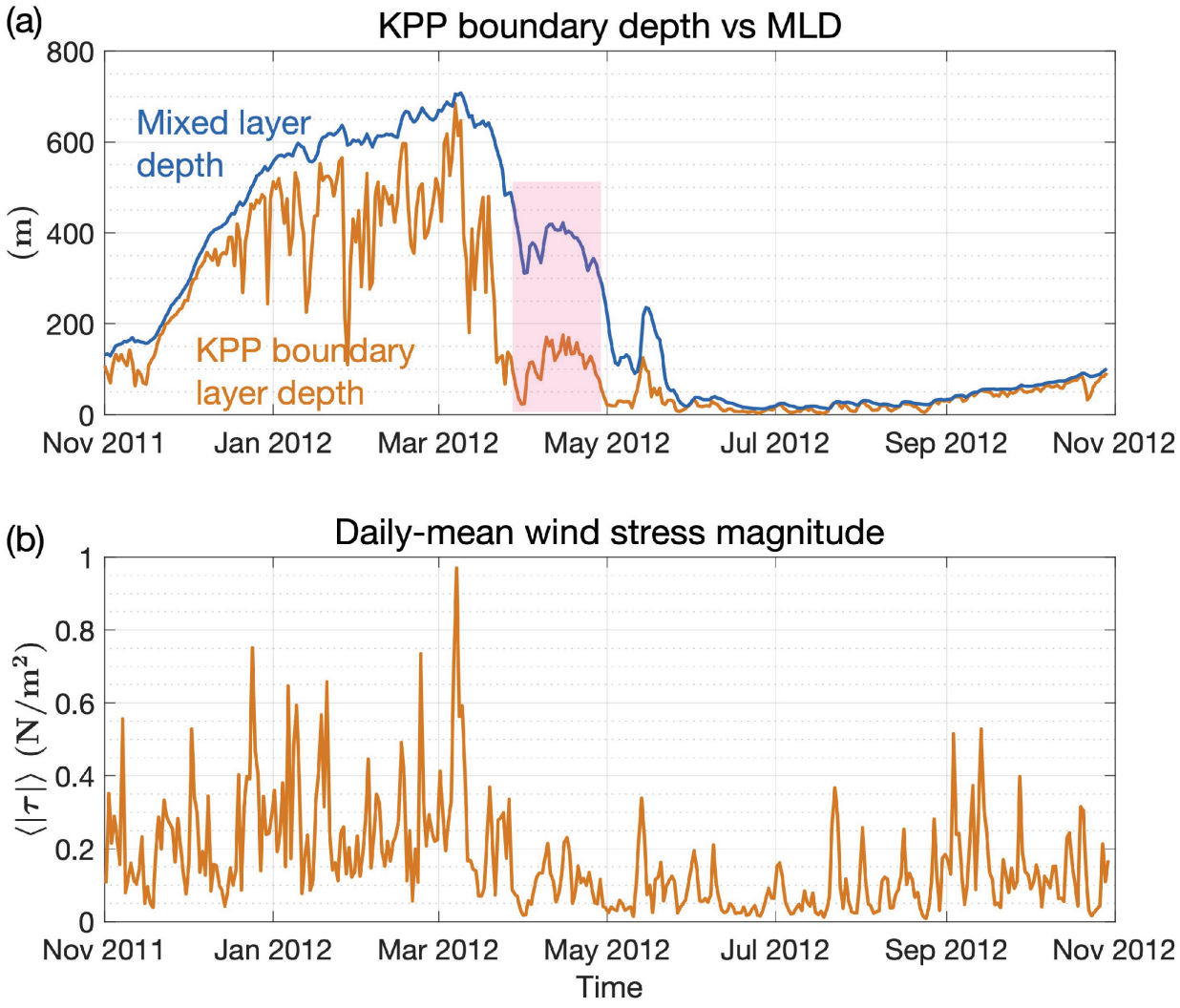

Figure S8. Time series of (a) KPP boundary layer depth compared with the mixed layer depth, and (b) wind stress magnitude, each averaged daily over the domain.